

RESEARCH ARTICLE

10.1002/2013JB010590

Key Points:

- Seismic source mechanisms of Vulcanian explosions
- Full moment tensor inversion of very long period seismic signals
- Opening of an ellipsoidal magma cavity associated with volcanic explosions

Correspondence to:

K. Kim,
keehoon@live.unc.edu

Citation:

Kim, K., J. M. Lees, and M. C. Ruiz (2014), Source mechanism of Vulcanian eruption at Tungurahua Volcano, Ecuador, derived from seismic moment tensor inversions, *J. Geophys. Res. Solid Earth*, 119, 1145–1164, doi:10.1002/2013JB010590.

Received 7 AUG 2013

Accepted 14 JAN 2014

Accepted article online 20 JAN 2014

Published online 13 FEB 2014

Source mechanism of Vulcanian eruption at Tungurahua Volcano, Ecuador, derived from seismic moment tensor inversions

Keehoon Kim¹, Jonathan M. Lees¹, and Mario C. Ruiz²¹Department of Geological Sciences, University of North Carolina at Chapel Hill, Chapel Hill, North Carolina, USA,²Instituto Geofísico de la Escuela Politécnica Nacional, Quito, Ecuador

Abstract Source mechanisms of explosive volcanic eruptions are critical for understanding magmatic plumbing systems and magma transport. Tungurahua is a large andesitic stratovolcano where seismoacoustic data has been recorded over several years. In May 2010, an energetic eruption cycle began with a midsize Vulcanian explosion followed by swarms of explosive eruptions. The five-station seismoacoustic network recorded significant seismic and infrasonic signals from the explosions. Source mechanisms of 50 explosion earthquakes associated with Vulcanian explosions during this eruptive period are investigated here. The source centroid locations and geometries of explosive signals in the 10–2 s band were determined by full-waveform moment tensor inversion. The observed waveforms are well explained by a combination of volumetric moment tensor components and a single, vertical, downward force component. The source centroids are positioned about 1.5 km below and about 320 m north of the active crater. Eigenvalue and eigenvector analysis indicates that the source geometries can be described by a subhorizontal, thin ellipsoid representing a sill-like magma accumulation. Resultant source time histories show a repetitive sequence of inflation and deflation from event to event, indicating identical source processes frequently occurred over the period. The inflation/deflation in the deep source region may be the result of crack opening. Volatile bubble growth at depth opens a pathway for gases to escape and triggers shallow explosions at the summit crater. The associated downward single force is interpreted as an exchange of linear momentum between the source and the surrounding region during the escaping gas flow.

1. Introduction

Quantitative analysis of seismic sources excited by volcanic processes can provide constraints on the geometry of magma plumbing systems, magma transport budgets, and temporal evolution of eruption processes. Portable broadband seismic instrumentation and digital networks have come into wide use in volcano monitoring. In recent years detailed monitoring has yielded seismic data of high enough quality to facilitate the quantification of seismic source mechanisms of volcanic eruptions, which ultimately will contribute to the assessment of volcanic behavior and associated hazard.

With the use of broadband seismometers, very long period (VLP) seismic signals with typical periods in the range of 2–100 s are frequently observed at many volcanoes. Because low-frequency waves suffer relatively less path distortion compared to the high frequency, VLP signals can provide a window into source processes related to volcanic activity. Systematic moment tensor inversion of VLP signal has been investigated where seismic source mechanisms were successfully extracted at a number of active volcanoes, including Kilauea [Ohminato *et al.*, 1998; Chouet *et al.*, 2010; Chouet and Dawson, 2011], Stromboli [Chouet *et al.*, 2003; Auger *et al.*, 2006], Popocatepetl [Chouet *et al.*, 2005], Asama [Ohminato *et al.*, 2006], Erebus [Aster *et al.*, 2008], Etna [Cannata *et al.*, 2009], Augustine [Dawson *et al.*, 2011], Tungurahua [Kumagai *et al.*, 2011], and Redoubt [Haney *et al.*, 2012]. Whereas tectonic earthquakes can be described by double-couple (DC) force systems, volumetric changes in seismic moment tensors were commonly observed at those volcanoes, occasionally with a single-force component [Chouet *et al.*, 2005; Ohminato *et al.*, 2006]. The volume change and single force component are typically interpreted as manifestations of inertial forces associated with the transport of magmatic fluids through volcano plumbing systems [Chouet and Matoza, 2013].

Explosive eruptions of Vulcanian type are characterized by the instantaneous ejection of volcanic bombs, ash, and gases and often associated with strong air shocks and seismic events. The seismic events

accompanying explosive Vulcanian eruptions, called “explosion earthquakes” hereafter, have also been inverted for moment tensor solution. At Mount St. Helens, 1980, it was shown that explosion earthquakes can be modeled by a combination of a single force and an implosive source [Kanamori *et al.*, 1984]. Tameguri *et al.* [2002] showed that an isotropic expansion occurred at a depth of 2 km before the explosive eruption at Mt. Sakurajima. Iguchi *et al.* [2008] also observed a triggering expansion preceding the surface explosion at Sakurajima, Suwanosejima, and Semeru Volcanoes. As explosion earthquakes are direct manifestations of dynamic conditions in the magma plumbing system, their moment tensor analysis can provide quantitative information about eruption processes such as the geometry of the conduit systems and the temporal evolution of seismic sources.

In this study, we investigate source mechanisms of Vulcanian eruptions at Tungurahua Volcano. Tungurahua (1.45°S, 78.43°W) is one of the most active andesitic volcanoes in Ecuador. Located on the Cordillera Real at the eastern border of the Interandean Valley, it has a 5023 m high summit with a 300 m wide crater, steep flanks, and extreme relief. Its current cone developed over the past 2300 years superimposed above two ancient edifices which were partially destroyed by large debris avalanches [Hall *et al.*, 1999]. Tungurahua has experienced at least 17 major eruptions in the last three millennia [Le Pennec *et al.*, 2006]. Since colonial times (1534), Tungurahua has exhibited five eruptive periods 1640–1645, 1773–1781, 1886–1888, 1916–1918, and 1999 to present [Hall *et al.*, 1999; Le Pennec *et al.*, 2006]. These eruptions were characterized by Vulcanian explosions and transitions between Vulcanian to Strombolian with mainly andesitic to dacitic compositions [Ruiz *et al.*, 2006].

During the recent eruptive period (1999 to present), volcanic activity at Tungurahua was dominated by episodic explosions with emissions of ash and gas through the vent in the summit crater. On 26 May 2010, an energetic eruption episode started with a strong explosion at the vent. Two days passed with no eruptive activity, then an even larger explosion occurred on 28 May, generating a 10 km high column and pyroclastic flows pouring down the volcano flanks. The volcano commenced explosive swarm activity including hundreds of events after 5 h of quiescence until 18 June, at which point the volcano returned to quiescence. Some explosions produced large noises resembling “cannon shot” which often vibrated windows and doors in the local area [Venzke *et al.*, 2002]. Extremely strong infrasound up to 200 Pa at 5 km distance was recorded with these explosions.

In this paper, explosion earthquakes associated with eruptive events during the May–June crises were inverted for seismic moment tensor. We used the linear inversion method proposed by Ohminato *et al.* [1998] to quantify the source mechanism of the explosion earthquakes. Synthetic waveforms were constructed by a superposition of Green's functions obtained for six moment tensor components and three single-force components. The geometry and temporal evolution of source mechanism is inferred here from the resultant moment tensor. The relationship between the explosion earthquakes and the vent explosion in the summit crater was further investigated using recorded infrasound data.

2. Data

Between 2006 and 2008 a network of five broadband seismoacoustic stations (Figure 1) was deployed by IG-EPN (Instituto Geofísico de la Escuela Politécnica Nacional, Ecuador), with support from Japan International Cooperation Agency (JICA) program to monitor Tungurahua for hazard mitigation and volcano research [Kumagai *et al.*, 2007]. Each station included a broadband seismometer (Guralp CMG-40T) with flat response to velocity from 30 s to 50 Hz and an ACO Type-7144/4144 acoustic sensor. The nominal infrasound sensor response was 0.1 to 100 Hz, with microphone sensitivity of 0.025 V/Pa and output voltage of ± 5 V. The sensors were set to record 893.5 Pa at full scale with sensitivity of -0.005593 V/Pa, and a 100 Hz low-pass filter was applied in the amplifier circuits. The microphones were designed specifically to record in harsh volcanic settings. Distances between the vent and stations ranged from 4.7 km at BPAT to 6.5 km at the furthest station BRUN.

A massive swarm of seismoacoustic events were recorded during the May–June crises of Tungurahua. An example of seismoacoustic records associated with the explosion is shown in Figure 2a. The observed seismoacoustic signals are characterized by (1) strong impulsive infrasound (~ 300 Pa) excited by explosions at the summit crater, (2) an emergent, compressional first-motion seismic arrival, and (3) following quasi-harmonic coda and volcanic tremor (or long-period waves). These data are representative of true ground displacement after being deconvolved for instrument response in the 0.02–30 s band. The VLP

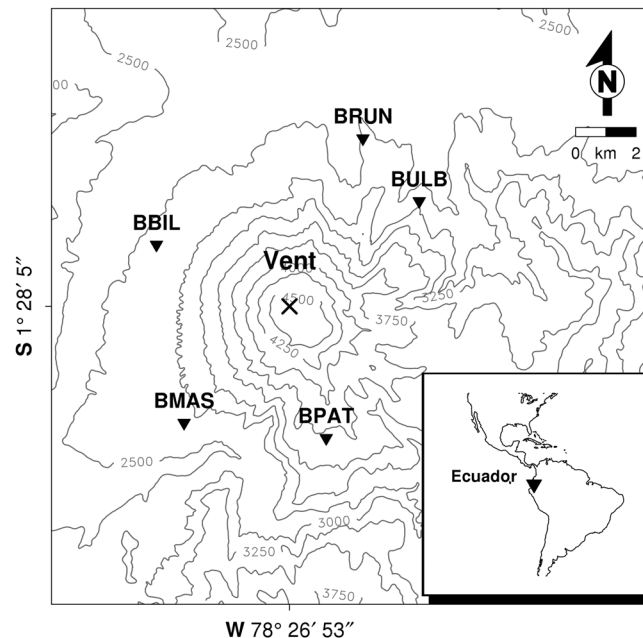


Figure 1. Map of Tungurahua volcano with the station geometry. Distances between the summit crater and stations range from 4.7 km at BPAT to 6.5 km at the farthest station BRUN.

signals of the first arrival motions (shown at 20 s in Figure 2a) were extracted by band-pass filtering the data in the 2–10 s band using fourth-order zero-phase-shift Butterworth filter. Overall VLP waveforms are impulsive (Figure 3a), but BPAT and BBIL stations show longer oscillatory tails than other stations. This may reflect local scattering or higher-frequency noises associated the explosion event. Even if unfiltered signals show clear compressional first motions, filtered VLP waveforms have dilatational motion (denoted in Figure 3a, arrows) just before the main compressional motion. This is caused by ringing effects of fourth-order Butterworth filter which rolls off rapidly around the cutoff frequency. The second-order Butterworth filter has less ringing effects in waveforms but introduces additional noises from higher-frequency band because of their slower roll-off, which markedly lowers signal-to-noise ratios of the signals.

Even if the representative event in Figure 2 shows distinct characteristics in seismic and acoustic signals, many of explosion earthquakes are obscure in waveforms. There may be two reasons for this. First is that the VLP band used in the study is partly overlapped with microseism noise band which typically has the band in 3 s to 7 s. Hence, if the explosion earthquakes are not large enough compared to microseismic noise, it is hard to recognize the entire waveforms of the first motion. Second is high-frequency energy associated with explosion earthquakes. Especially, BPAT and BBIL show marked noise near 1 Hz and make it hard to remove it completely from VLP band (2 s to 10 s). The high-frequency energy possibly comes from either local site effects or the surface explosion process that is not due to the VLP source.

In order to increase signal-to-noise ratio of the signals and reliability of moment tensor inversion, we here perform the inversion using a stacked data set from 50 similar events between 29 May and 1 June 2010 (Figure 4). Waveform similarity was quantified using waveform cross correlation. First, explosion earthquakes were selected, which were associated with surface explosions sharing the same characteristics described in Figure 2. We then computed the cross-correlation coefficient of vertical component at station BPAT between the prescreened events and the reference event in Figure 2 over a 16 s window that includes 8 s of preevent noise. This station was chosen because it is closest to the vent and showed the largest amplitudes for all events. Finally, 50 events were correlated with the master event at 0.8 or above. The waveforms for all stations were aligned to minimize the cross-correlation lags measured at BPAT and stacked. Before stacking the events, each station showed 14.3 ± 1.9 (15.7) dB, 15.6 ± 2.8 (19.5) dB, 11.6 ± 2.9 (14.2) dB, 15.2 ± 3.8 (16.1) dB, and 15.6 ± 3.8 (16.5) dB of signal-to-noise ratios of vertical component for BPAT, BBIL, BMAS, BRUN, and BULB, respectively, with the stacked waveform versions in parentheses. Respective signal-to-noise ratios increased by 21–147%.

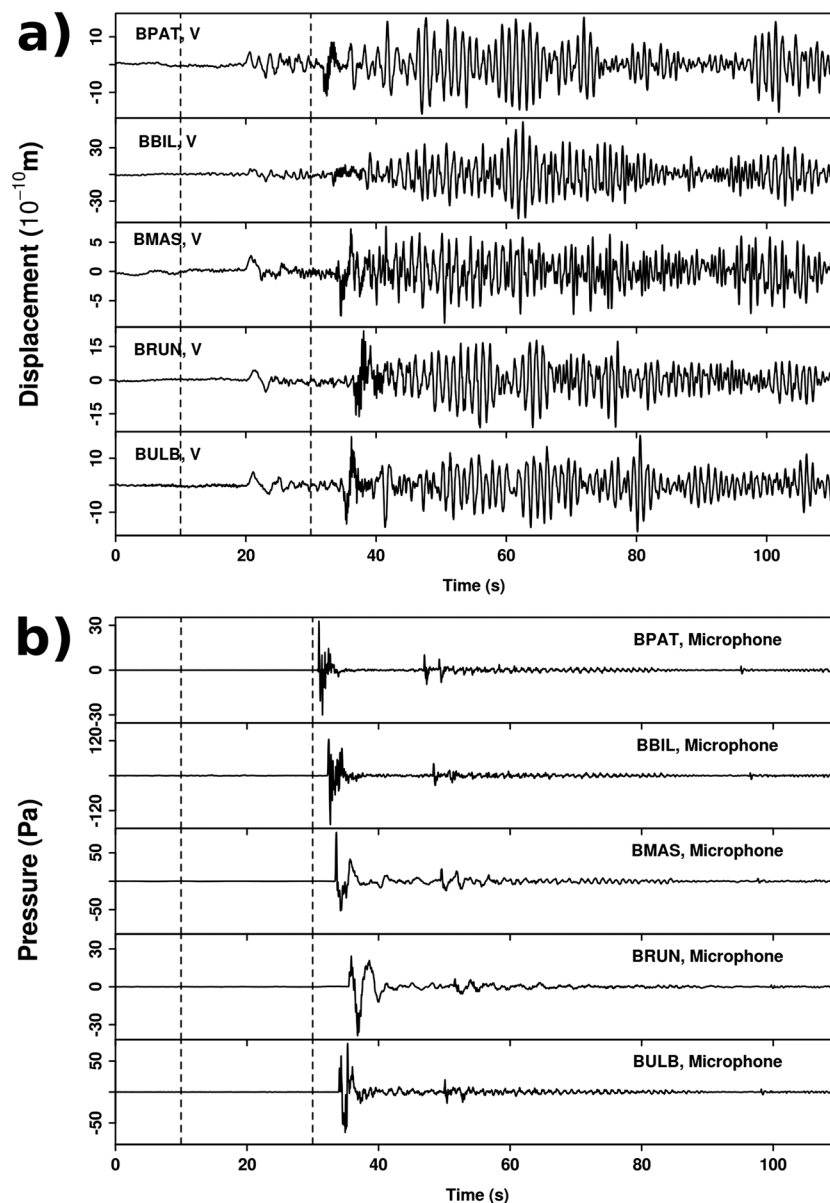


Figure 2. An example of seismoacoustic records associated with a crater explosion, which shows (a) vertical components and (b) infrasound for the reference event. Figure 2a shows the seismic signals which are characterized by a compressional P wave first motion emerging near 20 s and following quasi-harmonic coda and volcanic tremor. Figure 2b shows large impulsive waveform (~ 120 Pa) of infrasound that suggests a strong explosion at the summit crater.

Horizontal particle motions and east and north components of the stacked VLP waveforms are shown in Figure 5. Early part of motions (denoted by Figure 5, red lines) are elliptical or rectilinear pointing to the summit crater. Later part of motions, however, shows more complicated motions including transverse components. This may reflect local scattering and surface wave phases. The rectilinear motion of the early part of signal may be useful for approximating epicentral source location indicating that the VLP source is located near the summit crater. However, since topography can greatly influence waveforms, waveform modeling is required to clearly identify the source location [Neuberg and Pointer, 2000].

In this study, we applied inversion to stacked data and 10 explosion earthquakes showing high cross-correlation values (> 0.9) with respect to the reference event in Figure 2. The moment tensor inversion technique proposed by Ohminato *et al.* [1998] was used to extract source mechanisms represented by six moments and three single forces. High cross-correlation values among 50 events over May–June crises suggests a common explosive source process. We here present source parameters obtained only for 10

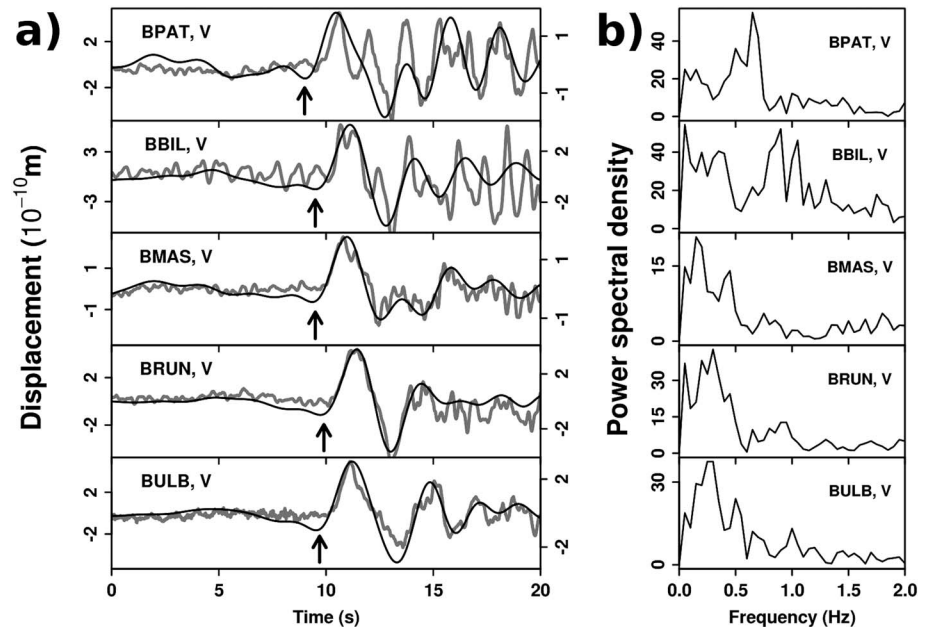


Figure 3. Band-pass filtered signals (10 s to 2 s) and power spectra of the first compressional motion between two vertical dashed lines in Figure 2. (a) The signals are representative of true ground displacement after being deconvolved for instrument response. Fourth-order zero-phase-shift Butterworth filter in 2–10 s band is used for band-pass filtering, and dilatational motions (indicated by arrows) are due to ringing effects of rapid roll-off around the cutoff frequency. (b) The signals showing impulsive waveforms have significant energy from 10 s to 2 s.

events (Table 2), and a full description, including source time function, is provided only for the stacked signal because all 10 events share common characteristics in the moment tensor solution; thus, an analysis of a representative event is adequate to describe the overall source mechanism.

3. Moment Tensor Inversion

The seismic displacement field can be expressed by a convolution of the Green’s function with the source terms [Chouet, 1996],

$$u_n(t) = F_p(t) * G_{np}(t) + M_{pq}(t) * G_{np,q}(t) \quad p, q = x, y, z, \quad (1)$$

where $u_n(t)$ is the n component of seismic displacement at a station at time t , $F_p(t)$ is the time history of the force applied in the p direction, $M_{pq}(t)$ is the time history of the pq component of the moment tensor, and $G_{np}(t)$ is the Green tensor which relates the n component of displacement at the receiver position with the p component of impulsive force at the source position. The notation q indicates spatial differentiation with respect to the q coordinate and the symbol $*$ denotes convolution. If we form the column vector \mathbf{d} that contains the displacement components at all stations and column vector \mathbf{m} containing the moment tensor and single force components, equation (1) can be rewritten in matrix form [Ohminato et al., 1998],

$$\mathbf{d} = \mathbf{Gm}. \quad (2)$$

Equation (2) is iteratively solved for \mathbf{m} using the sparse linear equations and least square problems algorithm, widely used for solving large, sparse, and ill-posed linear system [Paige and Saunders, 1982].

The synthetic Green’s functions are generated with the three-dimensional finite difference method [Ohminato and Chouet, 1997] taking into account the 3-D topography of Tungurahua Volcano. As the number of grid nodes searched for source locations is quite large, reciprocal relations for Green’s functions were used to reduce the number of numerical simulations. Using reciprocity, the Green’s function at each source node was derived from Green’s functions at each receiver node in the network [Chouet et al., 2005]. Because the number of receiver is much less than the number of source nodes, use of the reciprocity reduces huge amount of computational time. We assume a homogeneous velocity and density structure, a compressional wave velocity $V_p = 3.5$ km/s, shear wave velocity $V_s = 2$ km/s, and density $\rho = 2650$ kg/m³ [Molina et

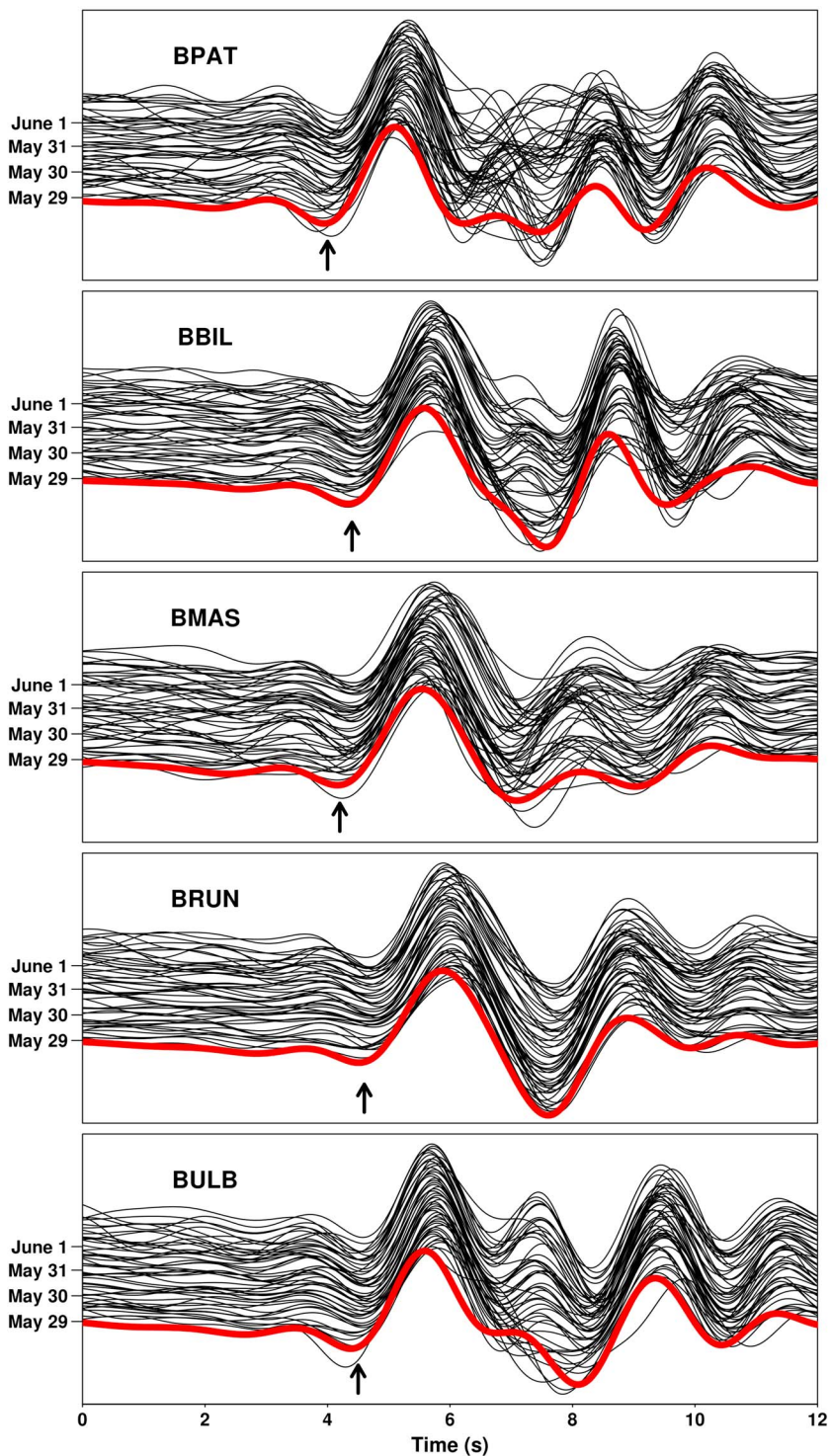


Figure 4. Vertical component displacement seismograms. Fifty events (black line) were selected based on high cross correlation with the reference event in Figure 3. Stacked vertical component seismogram is drawn by red line. The stacking increased signal-to-noise ratios by 21%–147% with respect to the individual signal. Dilatational motions caused by the band-pass filtering are indicated by black arrows.

al., 2005; Kumagai *et al.*, 2011]. The numerical Green’s functions are computed using a cosine smoothing function as a source excitation function,

$$S(t) = \begin{cases} \frac{1}{2} \left[1 - \cos\left(\frac{2\pi t}{t_p}\right) \right], & 0 \leq t \leq t_p \\ 0, & t > t_p. \end{cases} \quad (3)$$

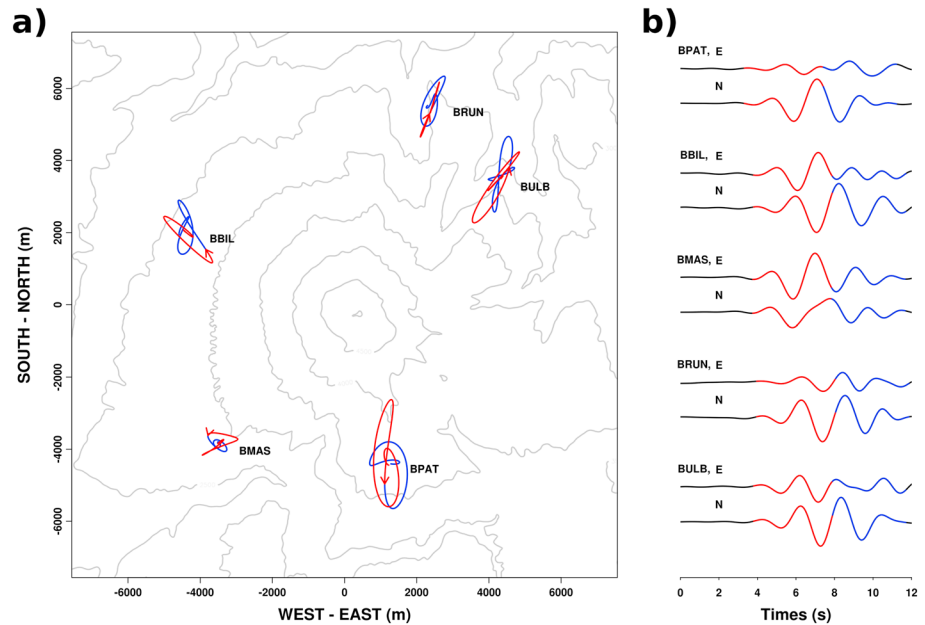


Figure 5. (a) Horizontal particle motion of the stacked VLP signal. (b) The records show east (E) and north (N) components of displacement seismogram, band-pass filtered in 10 s to 2 s. Early part of motions (denoted by red lines) are elliptical or rectilinear pointing to the summit crater. Later part of motions shows more complicated motions, including transversal components (blue lines).

where $t_p = 2$ s. The period of the smoothing function significantly influences the temporal resolution of the moment tensor solution and computation time for the Green's functions: the shorter the period, the higher the resolution of the resultant source time function. However, short-period smoothing functions require dense finite-difference grids for numerical stability, and, in turn, increase the computation time for Green's function. Since our data were band-pass filtered longer than 2 s, higher-frequency (< 2 s) components of the Green's function do not significantly contribute to the inversion result. Our computational domain is centered at the summit of Tungurahua and has lateral dimensions of 40×40 km, vertical dimensions of 40 km, which is sufficiently large to avoid spurious edge reflections. The node spacing is 80 m, yielding a 3-D mesh with $500 \times 500 \times 500$ nodes. While 25 nodes per wavelength are required for accurate modeling, 80 m spacing provides 50 nodes per wavelength ($2000 \text{ m/s} \times 2 \text{ s} = 4000 \text{ m}$) for periods considered in this study.

In order to assess the goodness of fit of the inversion, we use two definitions of squared errors as follows.

$$E_1 = \frac{1}{N_r} \sum_{n=1}^{N_r} \left[\frac{\sum_{p=1}^3 \sum_{\rho=1}^{N_s} (u_n^0(p\Delta t) - u_n^\rho(p\Delta t))^2}{\sum_{p=1}^3 \sum_{\rho=1}^{N_s} (u_n^0(p\Delta t))^2} \right], \quad (4)$$

and

$$E_2 = \frac{\sum_{n=1}^{N_r} \sum_{p=1}^{N_s} (u_n^0(p\Delta t) - u_n^\rho(p\Delta t))^2}{\sum_{n=1}^{N_r} \sum_{p=1}^{N_s} (u_n^0(p\Delta t))^2}, \quad (5)$$

where $u_n^0(p\Delta t)$ is the p th sample of the n th data trace, $u_n^\rho(p\Delta t)$ is the p th sample of the n th synthetic trace, N_r is the number of data traces, N_s is the number of samples in each trace, and N_r is the number of three-component stations. In equation (4), the squared error is normalized per station so that stations with weak-amplitude signals contribute equally to the squared error as stations with large-amplitude signals. In equation (5), the squared error is not normalized by station so that large-amplitude signals on the near-source stations dominate the squared error and the discrepancy between low-amplitude data and synthetics do not contribute significantly.

A grid search was conducted to determine the best fit source location. First, we searched 440 grid points (Figure 6) sparsely distributed over the $8000 \text{ m} \times 8000 \text{ m} \times 5000 \text{ m}$ gridded region in the east, north, and

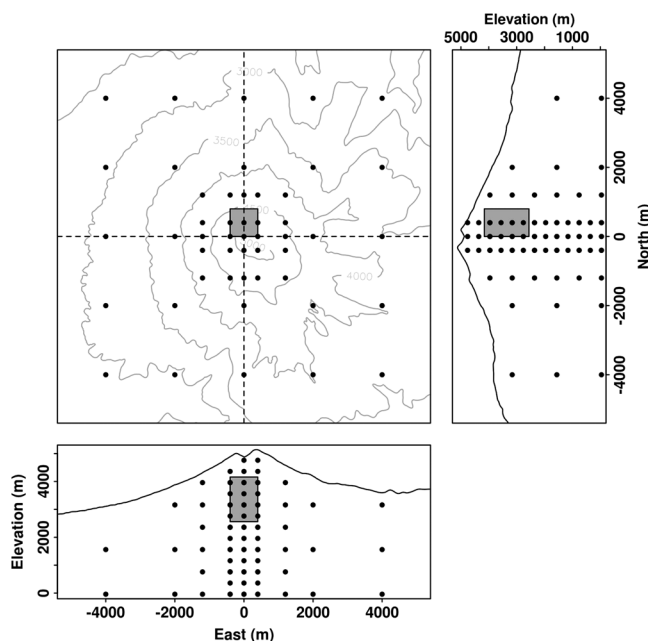


Figure 6. Horizontal, east-west and north-south vertical cross sections through the source domain. The positions of the cross sections are indicated by the dashed lines in map view. Dots indicate 440 grid nodes used in preliminary source location (see the text for details). The grid spacing is 400 m near the vent. The shaded rectangle indicates grid search domain in which grid nodes are densely distributed by 80 m. Final source location is determined within this region.

vertical directions, respectively. The grid spacing is finest near the vent (up to 400 m spacing) and coarser further away (up to 2000 m spacing). The least squares solutions to equation (2) are computed with respect to all grid points, and the preliminary source location is chosen by minimizing the squared error. Second, we defined densely distributed grid nodes surrounding the preliminary source position. In this region, grid nodes are spaced by 80 m apart in a uniform mesh extending to 800 m in the east-west and north-south directions and from 2560 to 4160 m in elevation. Final source location is determined by grid search within this region.

Since single forces can play an important role in volcanic processes, we consider three possible source mechanisms for the model parameters, \mathbf{m} : (1) six moments and three single forces, (2) six moments, and (3) three single forces. The optimum solution is chosen based on the squared error defined by equations (4) and (5), relevance of the free parameters used in the model, and physical significance of the resulting source mechanism. Relevance of the free parameters in each model is assessed by calculating Akaike's Information Criterion (AIC) [Akaike, 1974],

$$AIC = N_{\text{obs}} \ln E + 2N_{\text{par}}, \tag{6}$$

where $N_{\text{obs}} = 3 \times N_r N_s$ is the number of independent data, E is the squared error defined by equations (4) and (5), $N_{\text{par}} = N_s \times$ (the number of source mechanisms) is the number of model parameters used to fit the data. The model is considered to be physically relevant if it minimizes both the squared error and AIC. Finally, physical plausibility of a moment tensor solution is considered. Consistent time history among all moment tensor components is required to make a plausible interpretation of the solution.

4. Result

4.1. Squared Error

Inversion errors for the selected events are listed in Table 1. Residual errors defined in equation (4) or equation (5) are calculated for three different source models: six moments plus three single forces (Model 1), six moments only (Model 2), and three single forces only (Model 3). Model 1 shows at least 10% lower residuals in E_1 and E_2 than for other two models. According to the residual reduction, waveforms of the explosion earthquakes are best described by the combination of six moments and three single forces (Figure 8). E_2 errors are about 2% lower than E_1 errors. This residual reduction is achieved by fitting larger-amplitude

Table 1. Residual Errors and Corresponding Akaike's Information Criterion

Event No ^a .	Model 1 ^b				Model 2		Model 3	
	E_1	AIC(E_1)	E_2	AIC(E_2)	E_1	AIC(E_1)	E_1	AIC(E_1)
Stacked	0.096	-3443	0.075	-4177	0.242	-1862	0.510	-823
1	0.101	-3276	0.085	-3801	0.254	-1707	0.499	-886
2 ^c	0.098	-3368	0.077	-4081	0.285	-1368	0.452	-1182
3	0.128	-2573	0.120	-2755	0.302	-1193	0.532	-691
4	0.111	-3005	0.084	-3837	0.272	-1501	0.490	-938
5	0.136	-2390	0.121	-2739	0.301	-1200	0.528	-718
6	0.133	-2457	0.113	-2953	0.273	-1490	0.527	-720
7	0.109	-3058	0.093	-3519	0.242	-1852	0.488	-950
8	0.153	-2023	0.137	-2363	0.304	-1174	0.536	-673
9	0.101	-3292	0.094	-3503	0.239	-1889	0.507	-835
10	0.090	-3618	0.082	-3918	0.248	-1782	0.457	-1148

^aThe event number denotes chronological order in Table 2.

^bModels 1, 2, and 3 are composed of six moments plus three forces, six moments only, and three forces only, respectively.

^cReference event used to compute cross-correlation coefficient.

traces in stations closer to the summit sacrificing goodness-of-fit to smaller-amplitude signals. The most appropriate model for source mechanisms, however, cannot be determined solely by residual reduction since the large number of free model parameters decrease residual errors of inversion. To evaluate influence of the number of free parameters on residual errors, AICs are computed according to equation (6). The source model with six moments and three single forces consistently yield the minimum AICs for all the events. The small AICs suggest that the reduction of residuals for Model 1 is not merely a numerical artifact caused by a large number of free parameters but attributed to physical relevance of all model parameters. Physical relevance of Model 1 is further justified by consistent waveforms among moment tensor components in Figure 9, which allows a plausible interpretation of the solution. Hence, we focus on investigating source mechanism represented by Model 1 in the following sections.

4.2. Source Location

Figure 7 shows the locations of source centroids for Model 1 and the distribution of residual errors (E_1 and E_2) of the stacked and 10 selected events (Table 2). Source centroids for the stacked data (Figure 7, red spheres) with the minimum error in E_1 and E_2 and isosurfaces (Figure 7, red surfaces) representing the 2.0% error increment above the minimum residuals are computed and projected on Figure 7 (side and bottom). The isosurfaces are obtained by interpolation between 80 m spacing grid points. Source centroids obtained using the minimum error, E_1 , are shown in Figure 7a. The minimum residual of the stacked data ($E_1 = 9.6\%$, Table 2) yields a source centroid located 3280 m above sea level (1520 m below the summit crater) and 320 m north of the crater. Shape and extent of the isosurface can provide a measure of the uncertainty in source location. Volume surrounded by the surface has horizontal dimensions of ~ 500 m and spans the range 2800–3700 m in elevation. The volume is elongated in the vertical directions implying that vertical uncertainty in source location is larger than horizontal. This may be due to the station configuration where the closest deployment is 4.7 km from the crater, resulting in relatively poorly constrained depth of hypocenter below the crater. Best fit source positions for the selected events (Figure 7, blue spheres) in Table 2 are also plotted in Figure 7a. Their hypocenter locations are consistent with that of the stacked signal within 2.0% error increment. In Figure 7b, best fitting source locations are obtained according to the E_2 error (equation 5). The hypocenter of the stacked data ($E_2 = 7.5\%$) is located 3360 m above sea level (1440 m below the crater) and 80 m east and 320 m north of the crater. This is 80 m east and 80 m above the best fitting point of E_1 error minimum. Isosurface for the 2.0% error increment above the best fitting point has horizontal dimension of about 500 m and vertical dimension of about 900 m. The shape and extent of this volume is similar to that of the volume obtained by E_1 residual error. Hypocenters for the 10 events using E_2 residual error are all located within the 2.0% error increment bound. Similarity in source location and misfit distribution between two different measures of residual error, E_1 and E_2 , indicates a stable inversion for the source location. Small error reduction ($\sim 2\%$, Table 1) between E_1 and E_2 minimum error further support the observation that the source centroid inversion is not solely governed by a few stations with larger amplitude. Even if the optimum solution

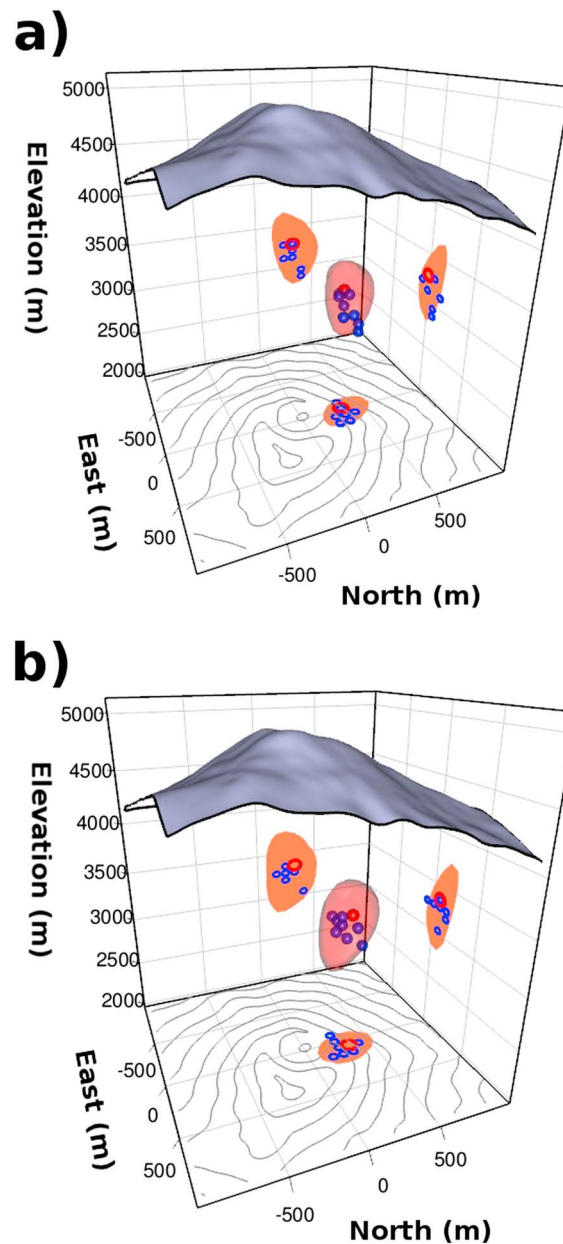


Figure 7. Best fit source location and error distribution for VLP events in Table 1. (a) Source locations obtained by minimizing E_1 error are plotted with red (stacked event) and blue spheres (10 events in Table 1). Isosurface (red surface) indicates the 2.0% error increment above the minimum residual. Source centroid and error outlines are projected on Figure 7 (side and bottom). (b) Same as Figure 7a but obtained by minimizing E_2 instead of E_1 . See the text for details.

coordinate is a measure of volume change (k) [Hudson *et al.*, 1989]. Source mechanisms for all the events involve dominant volume increases ($k = 0.81 \pm 0.02$). Volumetric changes are frequently observed with volcanic activity and are typically attributed to mass transport associated with volcanic processes [Miller *et al.*, 1998; Chouet *et al.*, 2003]. The combination of significant CLVD components ($T = -0.67 \pm 0.12$) and volume change indicates crack-like focal mechanisms. By assuming a Poisson ratio of $\nu = 1/3$, appropriate for volcanic rock [Murase and McBirney, 1973], source mechanisms of all the events lie along a trend between a pure crack and an isotropic explosion (Figure 11). The source-type plot shows only relative sizes of principal source types but does not contain any information about orientation of the source mechanism. In order to investigate directionality of the source mechanisms, the eigenvectors for the moment tensor solutions are

yielded from E_2 error shows lower misfit than E_1 error, we prefer the best fit solution from the E_1 error definition to avoid the influence of high-frequency noises consistently associated with station BPAT. Waveform fits between the stacked data and synthetic data obtained from the moment tensor solution at the source location show consistency (Figure 8). Overall fits are excellent, as demonstrated by the small residual error ($E_1 = 9.6\%$). The misfit errors of waveforms are normalized for each station so that stations with weak-amplitudes contribute equally to the moment tensor solution.

4.3. Source Time Function and Source Type
Source time functions of six moments and three single forces for the stacked data are shown in Figure 9. The waveforms are pulse-like and similar across moment and single force components. This similarity enables consistent interpretation of source mechanism from the source time functions. The volumetric components (M_{xx} , M_{yy} , and M_{zz}) clearly dominate off-diagonal components in the moment tensor. In addition, the vertical dipole, M_{zz} , dominates over the two horizontal dipoles, M_{xx} and M_{yy} . Time-varying eigenvectors of the moment tensors and total forces are plotted in Figure 10. The directions and amplitude ratios of the three eigenvectors are stable both before and after the peak amplitude. Principal components of the static moment tensor, which represents the time-varying moment tensor solutions, are extracted from peak-to-trough amplitudes of the three eigenvectors.

Figure 11 shows static moment tensors obtained from peak-to-trough amplitudes of the eigenvectors on a source-type plot [Hudson *et al.*, 1989]. The components of the moment tensors are listed in Table 2. The source-type plot displays characteristics of the moment tensor in terms of isotropic, double couple (DC), and compensated linear vector dipole (CLVD). The horizontal coordinate (T) describes the relative sizes of the DC ($T = 0$) and CLVD components ($T = \pm 1$), and the vertical coordi-

Table 2. Moment Tensor Inversion Result

No.	Date	Time	M_{xx}^a	M_{xy}	M_{xz}	M_{yy}	M_{yz}	M_{zz}	M_0^b	m_B^c
Stacked	-	-	+0.727	+0.013	-0.049	+0.679	+0.032	+0.989	$+0.940 \times 10^{10}$	2.9
1	05/29	02:50:01.69	+0.705	+0.011	-0.036	+0.654	+0.027	+0.994	$+1.415 \times 10^{10}$	2.9
2 ^d	05/29	11:26:25.79	+0.705	+0.011	-0.025	+0.664	+0.018	+0.997	$+1.048 \times 10^{10}$	2.9
3	05/29	13:49:39.21	+0.781	+0.003	-0.038	+0.731	+0.030	+0.990	$+0.916 \times 10^{10}$	2.9
4	05/30	01:14:18.83	+0.733	+0.013	-0.027	+0.671	+0.015	+0.997	$+1.043 \times 10^{10}$	2.9
5	05/30	03:33:11.70	+0.769	+0.005	-0.035	+0.714	+0.028	+0.992	$+1.069 \times 10^{10}$	2.9
6	05/30	19:16:26.98	+0.713	+0.007	-0.027	+0.657	+0.024	+0.996	$+1.307 \times 10^{10}$	2.9
7	05/31	04:17:29.14	+0.699	+0.009	-0.034	+0.659	+0.033	+0.993	$+0.824 \times 10^{10}$	2.8
8	05/31	08:18:41.83	+0.725	+0.001	-0.032	+0.684	+0.025	+0.994	$+1.090 \times 10^{10}$	2.9
9	06/01	00:50:42.72	+0.737	+0.009	-0.042	+0.699	+0.037	+0.989	$+1.157 \times 10^{10}$	2.9
10	06/01	05:46:17.98	+0.729	+0.018	-0.029	+0.678	+0.023	+0.996	$+0.635 \times 10^{10}$	2.8

^aAll the moment tensor components are normalized with respect to the scalar moment (M_0) event by event. Date is presented as month/date.

^bScalar moment (M_0^T , defined as proposed by Bowers and Hudson [1999, equation (11)].

^cBody wave magnitude determined by the relation between m_B and M_0 [Kanamori, 1983].

^dReference event used for computing cross-correlation coefficients.

presented in Figure 12. The orientations of the three principal axes ($T_1 > T_2 > T_3$) are remarkably consistent through all events. The direction of the longest principal axis (T_1) is tilted to the northwest by approximately 10° away from the vertical axis. The results from the source-type plot and the orientation of principal axes suggest that the source mechanisms of the explosion earthquakes were consistent among the selected events. While the dominant, vertical, principal axis, and source-type plot indicates involvement of subhorizontal crack-like source mechanism, the volume increase associated with the solutions are much larger than expected from a single, pure crack ($k = 0.65$). This result implies that true source geometry may be more complicated than a pure crack. In the next section, we discuss a possible source geometry in more detail.

4.4. Resolution Capability for Single Forces

Apparent single forces accompany the volumetric moments in our solutions (Figure 9). A vertical component (F_z) dominates the single forces. Timing of the negative peak in F_z coincides with that of the positive peaks in moment components implying that a downward force may be associated with the volumetric source process. The capability of the inversion method to decouple single forces from moment tensor components is assessed by a synthetic test. Due to the similarities of M_{zz} and F_z in the Green's functions, these components may be difficult to resolve when the station coverage is limited [Uhira and Takeo, 1994]. Synthetic waveforms are created using a point source at a depth of 1.6 km below the crater. The source mechanism is assumed to be a horizontal crack ($M_{xx} : M_{yy} : M_{zz} = 0.5 : 0.5 : 1$) with a downward single force ($F_z/M_{zz} = -0.125 \times 10^{-3}$), contributing $\sim 10\%$ of the waveform amplitudes. The single force and moment tensor components contribute equally to the observed signal amplitudes when the ratio (F_z/M_{zz}) is about 1.2×10^{-3} in this source/receiver configuration. Random noise signals are synthesized in the frequency

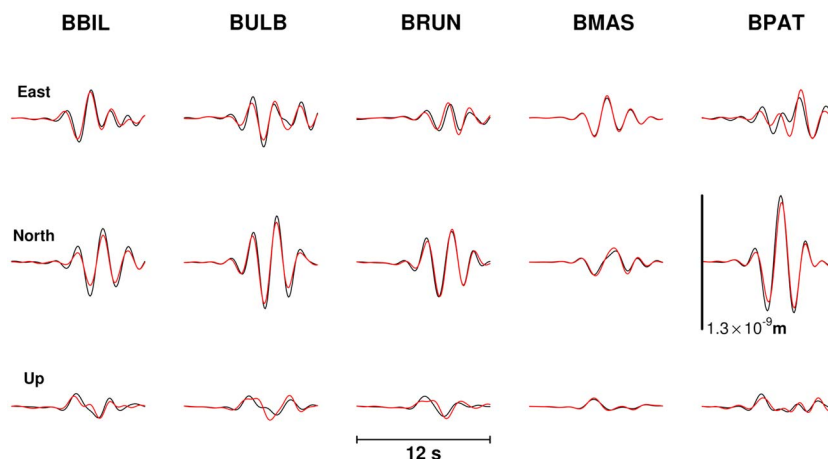


Figure 8. Waveform fit for stacked data (black lines). Synthetic waveforms (red lines) are obtained at the best fit source location in Figure 7a. Misfit errors (E_1 in equation (4)) of waveforms are normalized per station.

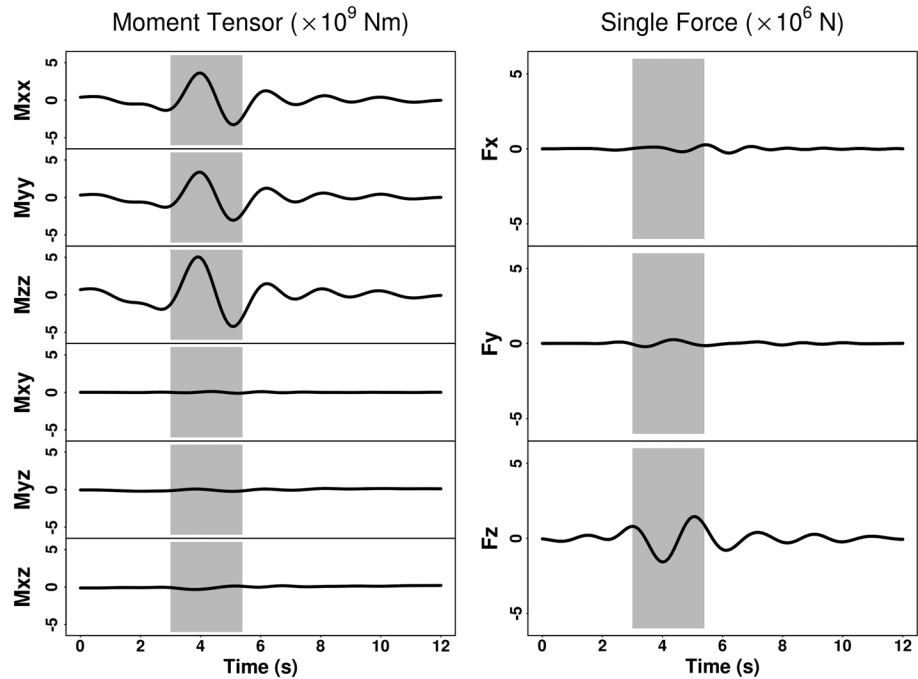


Figure 9. Source time functions of stacked data for Model 1. Volumetric components (M_{xx} , M_{yy} , and M_{zz}) and a downward force (F_z) are dominant in the moment tensor and single forces, respectively.

domain (2 s to 10 s) and transformed into the time domain. Amplitude of the noise is scaled and added to the synthetic data to achieve a signal-to-noise ratio of 15 dB, close to the observed signal. In this manner, five different data sets were created with random noise and inverted for moment tensor and single force solutions. The inversion results are shown in Figure 13.

Overall fitting of solutions to the known source time functions are poor because lower-frequency noise especially causes long-period oscillation in source time functions. The peak amplitudes of M_{zz} in inversion solutions range from 53% to 115% of those of the known source time functions (Figure 13). The ratios of M_{xx}/M_{zz} (0.49 ± 0.02), M_{yy}/M_{zz} (0.5 ± 0.02), and F_z/M_{zz} ($-0.15 \times 10^{-3} \pm 0.01 \times 10^{-3}$) are, however, consistent with the original ratios. Hence, if signal-to-noise ratio is high enough (> 15 dB), the downward single force (F_z) and the vertical dipole (M_{zz}) can be resolved using the existing station coverage even though the true amplitudes are uncertain.

Amplitude ratios of F_z/M_{zz} for the selected 10 events averaged $-0.28 \times 10^{-3} (\pm 0.03 \times 10^{-3}) \text{ m}^{-1}$. The stacked data shows $F_z/M_{zz} = -0.31 \times 10^{-3}$, contributing up to 25% of the waveform amplitudes. These amplitude ratios do not vary significantly between the events. Our synthetic test results and the consistent F_z/M_{zz} ratios between events strongly suggest that the observed downward single force is physically significant.

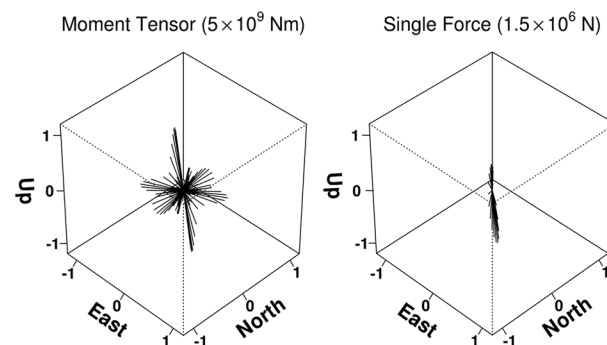


Figure 10. Three-dimensional representation of the eigenvectors (left) for the moment tensor and the resultant force (right) for time period shaded in Figure 9.

5. Discussion

5.1. Geometry of Source Region

Explosion earthquakes occurring over the May–June 2010, crises at Tungurahua show similar source mechanisms from their respective moment tensor solutions. They are characterized by constant volume increases and persistent directions of principal axes (Figures 11 and 12). Information about the source geometry can be retrieved from eigenvalues and eigenvectors (principal axes) of the moment tensors.

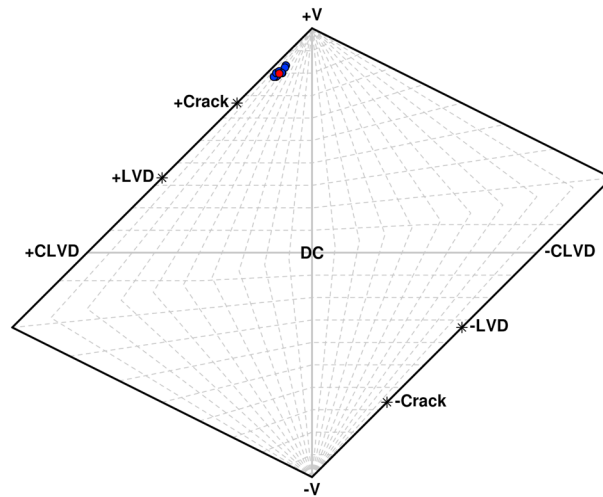


Figure 11. Source-type plot of Hudson. Source mechanisms for the events in Table 2 are plotted without regard to their orientation. Red and blue dots indicate stacked data and individual events, respectively. All source mechanisms lie between pure crack and isotropic explosion mechanisms [Hudson et al., 1989].

The most widely used method for reconstructing source geometry is to decompose the moment tensor into combinations of elementary source mechanisms, e.g., shear fault, CLVD, and inflation/deflation of crack, spherical cavity, and cylindrical cavity [Knopoff and Randall, 1970; Julian et al., 1998; Chouet, 1996]. Volume changes associated with volcanic processes have been explained typically by simple crack or spherical cavity models [Mogi, 1958; Ohminato et al., 1998; Chouet et al., 2003; Haney et al., 2012; Eyre et al., 2013]. If the volume changes were larger than those predicted from a single crack, additional intersecting cracks or cylindrical cavities were introduced to compensate for excess volume [Chouet et al., 2005, 2010; Lyons and Waite, 2011; Chouet and Dawson, 2011]. Since the composite model represents a general moment tensor in terms of discrete geometries alone, small perturbations on the moment tensor can yield quite different source geometries [Chouet, 1996]. The simple decomposition into the composite models is also highly nonunique.

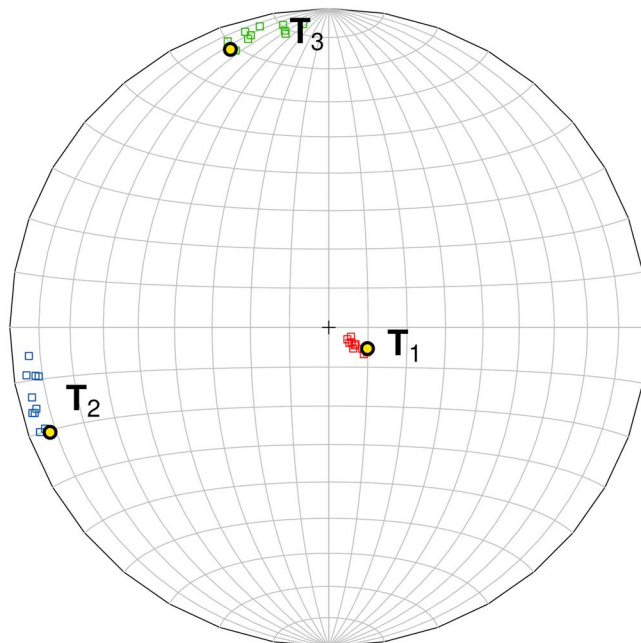


Figure 12. The eigenvectors of moment tensors projected on lower hemisphere. The orientation of the three principal axes ($T_1 > T_2 > T_3$) are remarkably consistent for all events. Eigenvectors for the stacked data are denoted by yellow circles.

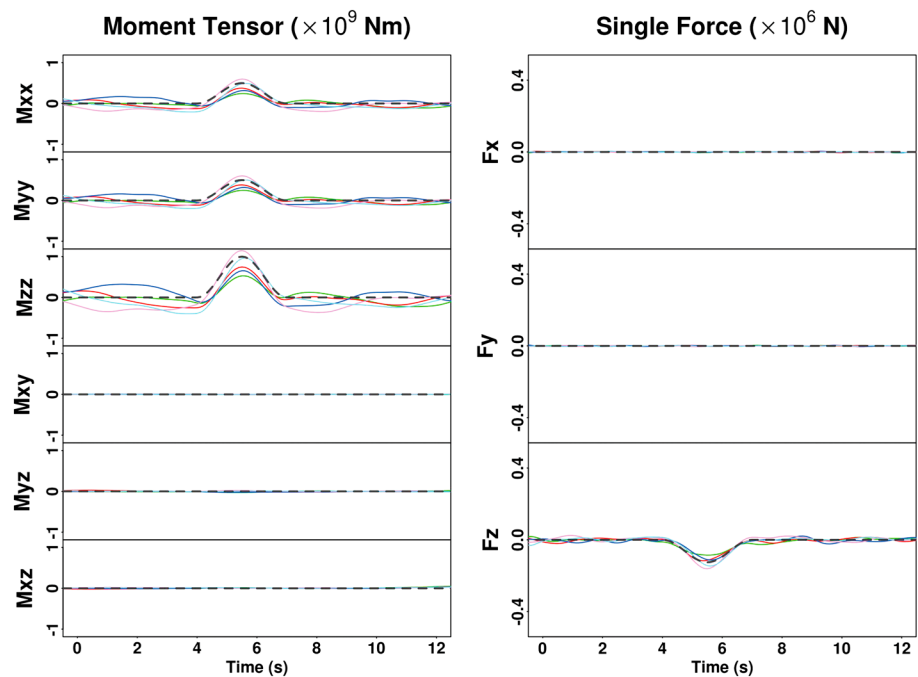


Figure 13. Numerical test of the capability of the inversion method to reconstruct known source time functions. Thick dashed lines are original source time functions, and solid lines indicate results of the inversion. The ratios of principal dipole components and the single force are $M_{xx} : M_{yy} : M_{zz} = 0.5 : 0.5 : 1$ and $F_z/M_{zz} = -0.125 \times 10^{-3}$ for true source time functions, and $M_{xx} : M_{yy} : M_{zz} = 0.49 : 0.5 : 1$ and $F_z/M_{zz} = -0.15 \times 10^{-3}$ for the results of the inversion (see the text for details).

Another way to represent the general moment tensor is to assume an ellipsoidal inclusion for inflation/deflation sources [Eshelby, 1957; Davis, 1986]. In contrast to the composite model, variations in cavity shapes between crack to sphere can be represented by a single triaxial ellipsoid without employing additional cavities. Since the ellipsoids are defined along a continuum with respect to the eigenvalue ratios of the moment tensor, small perturbations of the moment tensor results in correspondingly small changes in the geometrical shape (Figure 14). Whereas the composite model can describe fully general moment tensors by adding further cavities, only limited subsets of moment tensors can be represented by the single ellipsoid model (Figure 14). Since geometrical shapes corresponding to a moment tensor are not unique, a priori assumptions regarding the source geometry are important for retrieving appropriate source parameters.

In this study, moment tensor solutions are interpreted in terms of the single-ellipsoid model [Eshelby, 1957; Davis, 1986]. The elastic field due to an ellipsoidal inclusion in a half-space was treated by Davis [1986] by integrating distributions of point forces over the surface of the ellipsoid [Eshelby, 1957]. The pressurized ellipsoidal cavity can be described in terms of a moment tensor by point source approximation. Following Davis [1986], orientations of the ellipsoid are given by the eigenvectors of the moment tensor. The eigenvalues ($M_3 < M_2 < M_1$) are inversely related to the lengths of the ellipsoid axes ($a > b > c$), yielding ratios b/a and c/a . The eigenvalues are also proportional to the product between the source volume (V) and internal overpressure (ΔP) of the ellipsoid. Only a limited number of eigenvalue ratios (M_2/M_1 versus M_3/M_1) are allowable when obtaining ellipsoidal source shapes (denoted in Figure 14, shaded region). Pure cracks and spherical sources are special cases of ellipsoidal cavities.

Eigenvalue ratios for all events in Table 2 lie inside the shaded region of Figure 14, indicating that the solutions can be described by the single ellipsoidal model. The ratios of M_2/M_1 and M_3/M_1 range over 0.7–0.8 and 0.65–0.76, respectively. Furthermore, as noted above, orientations of eigenvectors are consistent across the events (Figure 12).

Consequent source parameters estimated for the pressurized ellipsoid model are listed in Table 3. Ellipsoidal shapes corresponding to the stacked waveforms are depicted in Figure 15 in which the center of the ellipsoids are assumed to be at the best fit source location obtained in the previous section. All of the ellipsoids inverted from the solutions are well constrained into asymmetric subhorizontal oblates. The oblates are elongated in the NW-SE direction. Due to the tight variances in the orientation and the ratios of ellipsoid

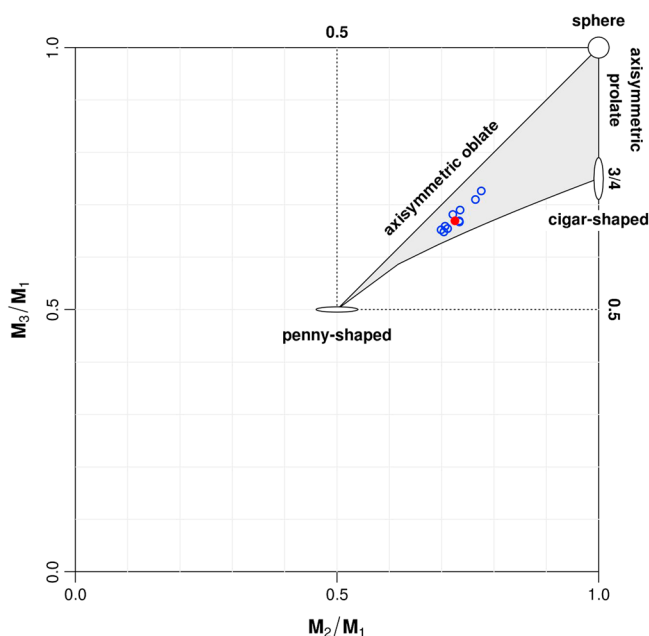


Figure 14. Ratios of eigenvalues M_3/M_1 and M_2/M_1 for all individual events (blue circle) and stacked data (red circle) assuming a Poisson ratio of $\nu = 1/3$. All the events are within the region allowed for ellipsoidal cavities. Ellipsoid for the stacked signal is depicted in Figure 15.

axes ($b/a = 0.54 \pm 0.09$ and $c/a = 0.29 \pm 0.06$), the stacked model ($b/a = 0.50$ and $c/a = 0.27$) well represents the overall shape of the ellipsoids. The absolute dimensions of the ellipsoids cannot be determined unambiguously since there is a trade-off between the volume and overpressure of the ellipsoidal cavities.

We compared our results to previous investigation on Tungurahua Volcano. *Molina et al.* [2005] performed tomographic inversion with volcano-tectonic (VT) earthquakes recorded from 1999 to 2003. A low-velocity zone ($V_p \sim 3$ km/s) was found under the NW flank at a depth of 2–2.5 km. Geological evidence suggests that the NW flank of Tungurahua was built by filling in of the caldera following an earlier sector collapse [*Hall et al.*, 1999]. *Molina et al.* [2005] interpreted the lower velocity zone as relatively low density, young, and poorly consolidated deposits filling the old caldera. Alternatively, the decrease in velocity may be attributed to fracture systems developed below the NW flank. The majority of the 263 deeper VT events used by *Molina et al.* [2005] were aligned vertically to a depth of 5 km beneath the crater. Above the 2 km depth level, however, most of the hypocenters were located below the west flank, spread ~ 500 m from the crater. *Kumagai et al.* [2011] located long volcanic tremors associated with an explosion event on 11 February 2010 by using vertical seismic amplitudes. The shallow tremors were located below the NW flank down to 2 km depth. Since volcanic tremor is often interpreted to be a manifestation of fluid-crack interactions, the tremor

locations suggest possible fracture systems under the NW flanks. Our moment tensor inversion indicates a subhorizontal oblate cavity (1.5 km below and 320 m north of the summit crater) representing a sill-like crack from a geological perspective. Hence, predeveloped crack systems under NW flank were likely reactivated during the May–June crises and served as a magma accumulation region that fed surface eruptions.

Table 3. Source Parameters Retrieved From the Moment Tensor Based on Ellipsoidal Model

Event No.	b/a^a	c/a	$V\Delta P^b$ ($N \cdot m$)
Stacked	0.505	0.275	6.6×10^8
1	0.435	0.225	9.3×10^8
2	0.530	0.270	7.1×10^8
3	0.685	0.410	7.4×10^8
4	0.430	0.245	7.4×10^8
5	0.630	0.370	8.4×10^8
6	0.445	0.235	8.8×10^8
7	0.510	0.255	5.5×10^8
8	0.650	0.335	7.9×10^8
9	0.640	0.345	8.6×10^8
10	0.465	0.260	4.5×10^8

^aLengths of the ellipsoid axes ($a > b > c$).

^bVolume (V) and internal overpressure (ΔP).

5.2. Source Dynamics

The source centroids imaged from inversion of explosion earthquakes were located at a depth of about 1.5 km. Our results indicate that the source locations and the source time histories

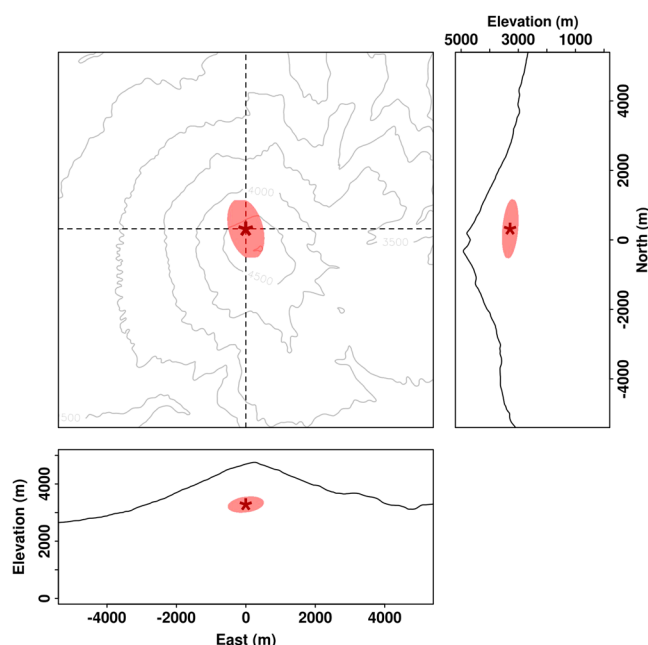


Figure 15. Resultant ellipsoidal cavity obtained from the stacked signal. Ellipsoids are centered at the best fit location in Figure 7a. Overall size is arbitrary, depending on the choice of V and Δp .

of the explosion earthquakes are similar from event to event, from which we infer that the same source region was activated repeatedly over the period of the volcanic crises in May 2010. The source geometries are thin subhorizontal ellipsoids geologically representing sill-like magma accumulations. Since these earthquakes produced Vulcanian explosions, ejecting volcanic bombs, ash, and gases, the source mechanisms of the events should be linked to observed activity at the vent.

Kanamori et al. [1984] proposed an equivalent force system appropriate for a volcanic eruption. In this model, sudden removal of a restraining cap above a pressurized magma cavity at shallow depth causes the volcanic explosion. The explosion is represented by combination of a downward vertical force and an implosive moment tensor. The downward vertical force is the reactive force of the volcanic jet or ejecta [Chouet, 1996]. The implosive moment tensor indicates a pressure decrease of the magma cavity as volcanic gases are released. Many volcanic eruptions associated with remarkable deflation at a shallow magma reservoir were interpreted using this model [Kanamori et al., 1984; Nishimura, 1998; Ohminato, 2006; Zobin et al., 2006; Cruz-Atienza et al., 2001]. In these cases, the burst of the conduit lids were attributed directly to the source of explosion earthquakes. Kanamori's model was adapted by *Uhira and Takeo* [1994] to account for the source mechanism of deep explosions at Sakurajima. A magma reservoir with small channel to the vent was placed at a depth of a few kilometers. Observed seismic waves were explained by an implosive moment tensor and a downward single force representing upward gas flow. *Tameguri et al.* [2002] suggested that explosive eruptions can be triggered by pressure waves generated by an initial, deeper, seismic source. Explosive earthquakes preceding the surface explosions at Sakurajima suggested that explosions at the crater were generated by isotropic expansions at a depth of 2 km [Tameguri et al., 2002]. Deep explosive earthquakes preceding the eruptive activity at Sakurajima, Suwanosejima, and Semeru Volcanoes have also been observed to follow a similar trend [Ishihara, 1985; Iguchi et al., 2008]. According to this model [Tameguri et al., 2002], a pressure wave is induced by fluctuations in the magma cavity and propagates through the conduit to the crater, triggering a surface explosion. The initial pressure disturbance can be caused by the burst of a gas bubble. The burst of a gas bubble opens a pathway for gases to escape, starting upward gas flow, thus causing a pressure drop in the deeper source region [Uhira and Takeo, 1994].

Our moment tensor analysis of the explosion earthquakes indicate abrupt pressure increases followed by rapid decreases in the magma cavity at a depth of 1.5 km. This source time history is well explained by Tameguri's model. The upward gas flow may explain the downward single force that coincides with the inflation in the moment tensor solution (Figure 9). A single force on the Earth can be generated by an exchange of linear momentum between the source volume and the surrounding region [Chouet et al., 2005]. The

overpressured gas and magma are forced into the vertical conduit that connects the magma cavity to the surface crater, and the resultant upward acceleration is represented by a downward single force.

The dynamics of pressure fluctuations observed in the source time function may be explained by diffusive bubble growth in magma. Using Henry's law and assuming a closed conduit (40 MPa, lithostatic pressure at 1.5 km depth) and Henry's constant of 9×10^{-12} (basaltic magma) – 1.6×10^{-11} (rhyolitic magma) [Nishimura, 2004], water concentration in silicate melts at a depth of 1.5 km is about 1.8–2.5 wt %. Magmas containing 1.8–2.5 wt % water can start to exsolve water at this depth. Amphiboles represent the phase most indicative of volatile abundance; however, they are not found in recent volcanic products from Tungurahua [Kumagai *et al.*, 2010], suggesting that the water content of the magma is less than 3–4 wt % [Cashman, 2004]. Based on simulations of diffusive bubble growth in magmas the timescale for bubble growth to its final equilibrium size varies from 22 s for basaltic magma (4.0 wt % water, 50 MPa confining pressure) to 1.2×10^4 s for rhyolitic magma (8.0 wt % water, 50 MPa confining pressure) [see Prousevitch *et al.*, 1993, Table 2]. Low volatile contents also significantly decrease the bubble growth rate. Assuming 1.8–2.5 wt % water concentration in magma, the time for complete growth of a bubble should be much longer than 22 s. This timescale is much longer than the few seconds observed in the VLP signals presented here. Alternatively, this rapid pressure fluctuation may be accounted for by crack or plug opening of the magma reservoir. Recall that the moment tensor solution is proportional to the volume (V) of the magma cavity and internal overpressure ($\Delta P = P_{in} - P_f$), where P_{in} is the pressure exerted on the internal wall of the cavity, and P_f is the confining pressure on the cavity. As bubbles grow in magma, the internal pressure will increase gradually. When the internal pressure exceeds the material strength of the plug, the plug will rupture or the crack will open. This opening will drop the confining pressure instantaneously, resulting in an abrupt increase of internal overpressure. Decrease of the internal overpressure will be followed by escape of gas bubbles and recovery of the confining pressure. Assuming that the semimajor axis of the ellipsoidal cavity obtained from stacked event (Table 3) is in the range $10 \text{ m} < a < 20 \text{ m}$, the volume of the cavity and overpressure will vary by $581 \text{ m}^3 < V < 4653 \text{ m}^3$ and $1.1 \text{ MPa} > \Delta p > 0.14 \text{ MPa}$, respectively, according to the moment tensor solution.

To show the connection between the earthquake sources and their surface manifestation we compare arrival times of seismic and acoustic waves. Onset times of seismic events are defined as the time when the moment tensor solutions exhibit peak amplitude in the source time history (Figure 9). Onset times of explosions are inferred from arrival times of infrasound on the five stations by assuming a constant sound velocity:

$$t_i^o = t_i^a - \frac{d_i}{c}, \quad (7)$$

where t_i^o is the origin time derived at the i th station, d_i is the distance from the summit crater to the i th station, t_i^a is the arrival time at i th station, and c is the atmospheric sound speed. The sound speed is assumed to be 340 m/s, appropriate for the average atmospheric temperature (15°C) in May at Tungurahua. (An error of ± 5 m/s in sound speed can change the traveltime at 5 km distant stations by ± 0.2 s.) The best fit origin time is selected to minimize the variance of t_i^o among the five stations. We determined origin times for the 10 events in Table 2 (Figure 16, traveltime curves are indicated by dashed lines). The origin time of infrasonic waves is 0.8 ± 0.3 s earlier than the observed onset estimates of the explosion earthquakes. If we assume that shock waves, however, were produced by the explosion, we must correspondingly adjust the infrasound origin times indicating a later arrival than those obtained assuming a simple constant velocity (Figure 16).

Observations of shock waves are commonly associated with Vulcanian explosions [Ishihara, 1985; Gottschämmer and Surono, 2000]. Shock waves are nonlinear waves excited by supersonic flows or extreme variations of pressure over short time periods. The higher the overpressure at the shock front, the greater the velocity of the shock wave. Initially, shock velocities may be quite high, several times the speed of sound in air. As shock waves propagate away from the vent, the pressure at the shock front decreases and the velocity falls off accordingly, approaching ambient sound speeds [Glasstone, 1964]. Under these circumstances traveltime curves for shock waves will not follow a simple linear trend and estimating the appropriate origin time may be difficult. At Tungurahua, however, all stations are situated further than 4.8 km from the vent, where the shock wave velocity has most likely decreased to the ambient sound speed. For the purposes of this study we will assume a constant shock velocity of 560 m/s (originally measured at Bromo Volcano,

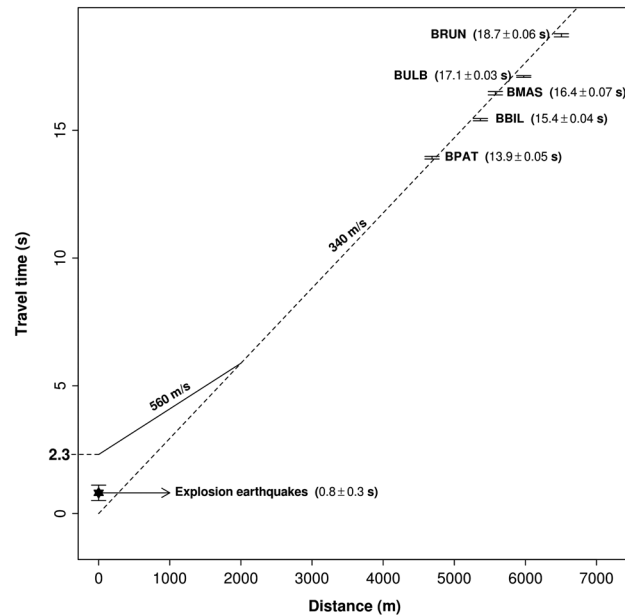


Figure 16. Traveltime curves for the infrasound excited by the explosion at the crater. Origin times are calculated for all events by assuming constant sound speed (340 m/s). Mean arrival times and standard deviations are denoted per station.

Indonesia, 2 km away from the vent [Gottschämmer and Surono, 2000]). Using this estimate, the surface explosions at Tungurahua occur 1.5 ± 0.3 s later than associated explosion earthquakes (Figure 16).

While the predicted origin times, based on linear infrasound projections, suggest that explosion earthquakes occur close to the onset of the surface explosions, we reject that possibility based on the moment tensor inversion solutions. We note that the time sequence of the two events (deep seismic, shallow explosion) is ambiguous because of the possible presence, and accelerated acoustic speeds, of shock waves. Considering the fact that shock waves are commonly accompanied by Vulcanian explosions and the source

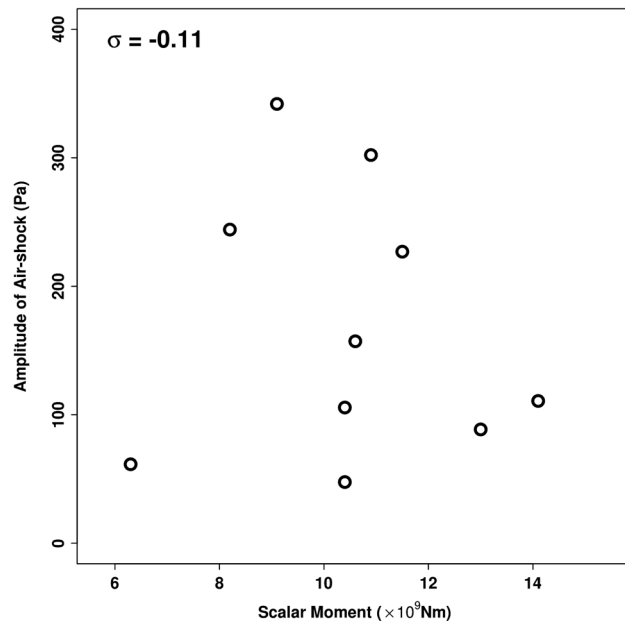


Figure 17. Comparison of scalar moments to amplitude of air shock excited by explosions at the summit crater (Table 2). The pressure was measured at BBIL consistently showing the largest amplitude among the stations. No significant correlation is observed, indicating that the signals (infrasound and seismic) emanate from two different event phenomena.

mechanism of the explosion earthquakes suggest a deep-triggering pressure increase, the observed surface explosions most likely occur later than the associated seismic events.

We compared the amplitude of infrasound with the corresponding seismic moments in Figure 17. Pressure recorded at station BBIL is used to represent the energy of the explosive eruption at the vent because of its large amplitude. Amplitudes of infrasound observed from the 10 events show virtually no correlation ($\sigma = -0.11$) with the seismic moments. This suggests that the signals (infrasound and seismic) emanate from two, different, event phenomena.

6. Conclusion

We investigate source mechanisms of Vulcanian explosions at Tungurahua Volcano. Low-frequency seismic events associated with explosive eruptions are inverted for the seismic moment tensors and single forces. The results point to a source 1.5 km below and 320 m north of the summit crater. The moment tensor solutions are represented by an ellipsoidal pressurized cavity. The semiminor axis of the ellipsoid is almost vertical indicating a sill-like magma cavity. Comparison of magnitudes of the moment tensors and corresponding air shocks shows no correlation, suggesting the seismic and acoustic signals emanate from two different event phenomena. If we assume that shock waves accompany surface explosions and thus introduce an accelerated acoustic wave, the measured time delay between the predicted origins of acoustic relative to the seismic waves is strong evidence that surface explosions at Tungurahua are triggered by deep seismic events in the magma reservoir. Analysis suggests that inflation/deflation in the deep source regions are the result of crack openings. Pressure increase by bubble growth in the rising magma opens a pathway for gases to escape and subsequently triggers surface explosion. The downward single force in our solution may be produced by an exchange of linear momentum between the source and the surrounding region during the escaping gas flow.

Acknowledgments

This research was supported by the National Science Foundation Grant OIA-1125185 and EAR-0838395, and SENESCYT Project PIN-08 Fortalecimiento del Sistema Nacional de Sismología y Vulcanología. We thank Hiroyuki Kumagai for establishing the high-quality seismoacoustic network at Tungurahua through cooperation between the Japanese JICA program and Fortalecimiento del Sistema de Monitoreo sísmico y volcánicos. We also thank the authorities and staff of the Instituto Geofísico and Observatorio Vulcanológico del Tungurahua for sharing data and providing support.

References

- Akaike, H. (1974), A new look at the statistical model identification, *IEEE T. Automat. Contr.*, *19*(6), 716–723, doi:10.1109/TAC.1974.1100705.
- Aster, R., D. Zandomenighi, S. Mah, S. McNamara, D. Henderson, H. Knox, and K. Jones (2008), Moment tensor inversion of very long period seismic signals from strombolian eruptions of Erebus Volcano, *J. Volcanol. Geotherm. Res.*, *177*, 635–647, doi:10.1016/j.jvolgeores.2008.08.013.
- Auger, E., L. D'Auria, M. Martini, B. Chouet, and P. Dawson (2006), Real-time monitoring and massive inversion of source parameters of very long period seismic signals: An application to Stromboli Volcano, Italy, *Geophys. Res. Lett.*, *33*(4), L04301, doi:10.1029/2005GL024703.
- Bowers, D., and J. A. Hudson (1999), Defining the scalar moment of a seismic source with a general moment tensor, *Bull. Seismol. Soc. Am.*, *89*(5), 1390–1394.
- Cannata, A., M. Hellweg, G. D. Grazia, S. Ford, S. Alparone, S. Gresta, P. Montalto, and D. Patan (2009), Long period and very long period events at Mt. Etna Volcano: Characteristics, variability and causality, and implications for their sources, *J. Volcanol. Geotherm. Res.*, *187*, 227–249, doi:10.1016/j.jvolgeores.2009.09.007.
- Cashman, K. V. (2004), Volatile controls on magma ascent and eruption, in *The State of the Planet: Frontiers and Challenges in Geophysics*, edited by R. S. J. Sparks and C. J. Hawkesworth, pp. 109–124, AGU, Washington, D. C., doi:10.1029/150GM10.
- Chouet, B. (1996), New methods and future trends in seismological volcano monitoring, in *Monitoring and Mitigation of Volcano Hazards*, edited by R. Scarpa and R. Tilling, pp. 23–97, Springer, Berlin, Germany.
- Chouet, B., and P. Dawson (2011), Shallow conduit system at Kilauea Volcano, Hawaii, revealed by seismic signals associated with degassing bursts, *J. Geophys. Res.*, *116*, B12317, doi:10.1029/2011JB008677.
- Chouet, B., P. Dawson, T. Ohminato, M. Martini, G. Saccorotti, F. Giudicepietro, G. De Luca, G. Milana, and R. Scarpa (2003), Source mechanisms of explosions at Stromboli Volcano, Italy, determined from moment-tensor inversions of very-long-period data, *J. Geophys. Res.*, *108*(B1), 2019, doi:10.1029/2002JB001919.
- Chouet, B., P. Dawson, and A. Arciniega-Ceballos (2005), Source mechanism of Vulcanian degassing at Popocatepétl Volcano, Mexico, determined from waveform inversions of very long period signals, *J. Geophys. Res.*, *110*, B07301, doi:10.1029/2004JB003524.
- Chouet, B. A., and R. S. Matoza (2013), A multi-decadal view of seismic methods for detecting precursors of magma movement and eruption, *J. Volcanol. Geotherm. Res.*, *252*, 108–175, doi:10.1016/j.jvolgeores.2012.11.013.
- Chouet, B. A., P. B. Dawson, M. R. James, and S. J. Lane (2010), Seismic source mechanism of degassing bursts at Kilauea Volcano, Hawaii: Results from waveform inversion in the 10–50 s band, *J. Geophys. Res.*, *115*, B09311, doi:10.1029/2009JB006661.
- Cruz-Atienza, V. M., J. F. Pacheco, S. K. Singh, N. M. Shapiro, C. Valds, and A. Iglesias (2001), Size of Popocatepétl volcano explosions (1997–2001) from waveform inversion, *Geophys. Res. Lett.*, *28*(21), 4027–4030, doi:10.1029/2001GL013207.
- Davis, P. M. (1986), Surface deformation due to inflation of an arbitrarily oriented triaxial ellipsoidal cavity in an elastic half-space, with reference to Kilauea Volcano, Hawaii, *J. Geophys. Res.*, *91*(B7), 7429–7438, doi:10.1029/JB091iB07p07429.
- Dawson, P. B., B. A. Chouet, and J. Power (2011), Determining the seismic source mechanism and location for an explosive eruption with limited observational data: Augustine Volcano, Alaska, *Geophys. Res. Lett.*, *38*, L03302, doi:10.1029/2010GL045977.
- Eshelby, J. D. (1957), The determination of the elastic field of an ellipsoidal inclusion, and related problems, *Proc. R. Soc. London, Ser. A*, *241*(1226), 376–396, doi:10.1098/rspa.1957.0133.
- Eyre, T. S., C. J. Bean, L. D. Barros, G. S. O'Brien, F. Martini, I. Lokmer, M. M. Mora, J. F. Pacheco, and G. J. Soto (2013), Moment tensor inversion for the source location and mechanism of long period (LP) seismic events from 2009 at Turrialba Volcano, Costa Rica, *J. Volcanol. Geotherm. Res.*, *258*, 215–223, doi:10.1016/j.jvolgeores.2013.04.016.

- Glasstone, S., (1964), The effects of nuclear weapons, *Tech. Rep.*, U.S. Department of Defense, Univ. of California, Santa Barbara, Calif. [Available at <http://www.fourmilab.ch/etexts/www/effects/>.]
- Gottschämmer, E., and I. Surono (2000), Locating tremor and shock sources recorded at Bromo Volcano, *J. Volcanol. Geotherm. Res.*, 101(1–2), 199–209, doi:10.1016/S0377-0273(00)00171-2.
- Hall, M. L., C. Robin, B. Beate, P. Mothes, and M. Monzier (1999), Tungurahua Volcano, Ecuador: Structure, eruptive history and hazards, *J. Volcanol. Geotherm. Res.*, 91(1), 1–21, doi:10.1016/S0377-0273(99)00047-5.
- Haney, M. M., B. A. Chouet, P. B. Dawson, and J. A. Power (2012), Source characterization for an explosion during the 2009 eruption of Redoubt Volcano from very-long-period seismic waves, *J. Volcanol. Geotherm. Res.*, 259, 77–88, doi:10.1016/j.jvolgeores.2012.04.018.
- Hudson, J. A., R. G. Pearce, and R. M. Rogers (1989), Source type plot for inversion of the moment tensor, *J. Geophys. Res.*, 94(B1), 765–774.
- Iguchi, M., H. Yakiwara, T. Tameguri, M. Hendrasto, and J. Hirabayashi (2008), Mechanism of explosive eruption revealed by geophysical observations at the Sakurajima, Suwanosejima and Semeru Volcanoes, *J. Volcanol. Geotherm. Res.*, 178, 1–9, doi:10.1016/j.jvolgeores.2007.10.010.
- Ishihara, K. (1985), Dynamical analysis of volcanic explosion, *J. Geodyn.*, 3(3), 327–349, doi:10.1016/0264-3707(85)90041-9.
- Julian, B. R., A. D. Miller, and G. R. Foulger (1998), Non-double-couple earthquakes 1. Theory, *Rev. Geophys.*, 36(4), 525–549.
- Kanamori, H. (1983), Magnitude scale and quantification of earthquakes, *Tectonophysics*, 93(3–4), 185–199, doi:10.1016/0040-1951(83)90273-1.
- Kanamori, H., J. W. Given, and T. Lay (1984), Analysis of seismic body waves excited by the Mount St. Helens eruption of May 18, 1980, *J. Geophys. Res.*, 89(B3), 1856–1866.
- Knopoff, L., and M. J. Randall (1970), The compensated linear-vector dipole: A possible mechanism for deep earthquakes, *J. Geophys. Res.*, 75(26), 4957–4963.
- Kumagai, H., et al. (2007), Enhancing volcano-monitoring capabilities in Ecuador, *EOS Trans. AGU*, 88, 245–246, doi:10.1029/2007EO230001.
- Kumagai, H., M. Nakano, T. Maeda, H. Yepes, P. Palacios, M. Ruiz, S. Arrais, M. Vaca, I. Molina, and T. Yamashima (2010), Broad-band seismic monitoring of active volcanoes using deterministic and stochastic approaches, *J. Geophys. Res.*, 115(B8), B08303, doi:10.1029/2009JB006889.
- Kumagai, H., P. Placios, M. Ruiz, H. Yepes, and T. Kozono (2011), Ascending seismic source during an explosive eruption at Tungurahua Volcano, Ecuador, *Geophys. Res. Lett.*, 38, L01306, doi:10.1029/2010GL045944.
- Le Pennec, J. L., D. Jaya, and J. van der Plicht (2006), Recurrence pattern of late Holocene eruptions at Tungurahua Volcano (Ecuador) revealed by radiocarbon dating of charcoal in pyroclastic flow deposits, paper presented at Internationale/ "Cities on Volcanoes", Quito, volume des résumés, 64.
- Lyons, J. J., and G. P. Waite (2011), Dynamics of explosive volcanism at Fuego Volcano imaged with very long period seismicity, *J. Geophys. Res.*, 116, B09303, doi:10.1029/2011JB008521.
- Miller, A. D., G. R. Foulger, and B. R. Julian (1998), Non-double-couple earthquakes 2. Observations, *Rev. Geophys.*, 36(4), 551–568.
- Mogi, K. (1958), Relations between the eruptions of various volcanoes and the deformations of the ground surfaces around them, *Bull. Earthq. Res. Inst.*, 36, 99–134.
- Molina, I., H. Kumagai, J.-L. L. Pennec, and M. Hall (2005), Three-dimensional P-wave velocity structure of Tungurahua Volcano, Ecuador, *J. Volcanol. Geotherm. Res.*, 147, 144–156, doi:10.1016/j.jvolgeores.2005.03.011.
- Murase, T., and A. McBirney (1973), Properties of some common igneous rocks and their melts at high temperatures, *Geol. Soc. Am. Bull.*, 84(11), 3563–3592.
- Neuberg, J., and T. Pointer (2000), Effects of volcano topography on seismic broad-band waveforms, *Geophys. J. Int.*, 143(1), 239–248, doi:10.1046/j.1365-246x.2000.00251.x.
- Nishimura, T. (1998), Source mechanisms of volcanic explosion earthquakes: Single force and implosive sources, *J. Volcanol. Geotherm. Res.*, 86(1), 97–106, doi:10.1016/S0377-0273(98)00088-2.
- Nishimura, T. (2004), Pressure recovery in magma due to bubble growth, *Geophys. Res. Lett.*, 31, L12613, doi:10.1029/2004GL019810.
- Ohminato, T. (2006), Characteristics and source modeling of broadband seismic signals associated with the hydrothermal system at Satsuma-Iwojima Volcano, Japan, *J. Volcanol. Geotherm. Res.*, 158, 467–490, doi:10.1016/j.jvolgeores.2006.08.004.
- Ohminato, T., and B. A. Chouet (1997), A free-surface boundary condition for including 3D topography in the finite-difference method, *Bull. Seismol. Soc. Am.*, 87(2), 494–515.
- Ohminato, T., B. A. Chouet, P. Dawson, and S. Kedar (1998), Waveform inversion of very long period impulsive signals associated with magmatic injection beneath Kilauea Volcano, Hawaii, *J. Geophys. Res.*, 103(B10), 23,839–23,862.
- Ohminato, T., M. Takeo, H. Kumagai, T. Yamashina, J. Oikawa, E. Koyama, H. Tsuji, and T. Urabe (2006), Vulcanian eruptions with dominant single force components observed during the Asama 2004 volcanic activity in Japan, *Earth Planets Space*, 58, 583–593.
- Paige, C. C., and M. A. Saunders (1982), Lsq: An algorithm for sparse linear equations and sparse least squares, *ACM Trans. Math. Softw.*, 8(1), 43–71, doi:10.1145/355984.355989.
- Prousevitch, A. A., D. L. Sahagian, and A. T. Anderson (1993), Dynamics of diffusive bubble growth in magmas: Isothermal case, *J. Geophys. Res.*, 98(B12), 22,283–22,307, doi:10.1029/93JB02027.
- Ruiz, M., J. Lees, and J. Johnson (2006), Source constraints of Tungurahua Volcano explosion events, *B. Volcanol.*, 68, 480–490.
- Tameguri, T., M. Iguchi, and K. Ishihara (2002), Mechanism of explosive eruptions from moment tensor analyses of explosion earthquakes at Sakurajima Volcano, Japan, *Bull. Volcanol. Soc. Jpn.*, 47(4), 197–215.
- Uhira, K., and M. Takeo (1994), The source of explosive eruptions of Sakurajima Volcano, Japan, *J. Geophys. Res.*, 99(B9), 17,775–17,789, doi:10.1029/94JB00990.
- Venzke, E., R. W. Wunderman, L. McClelland, T. Simkin, J. Luhr, L. Siebert, G. Mayberry, and S. Sennert (2002), Global volcanism, 1968 to the present. Smithsonian Institution, Global Volcanism Program Digital Information Series, GVP-4 (<http://www.volcano.si.edu/reports/>), Smithsonian Institution, Global Volcanism program digital information series.
- Zobin, V. M., C. Navarro, G. Reyes-Dávila, J. Orozco, M. Bretón, A. Tellez, G. Reyes-Alfaro, and H. Vázquez (2006), The methodology of quantification of volcanic explosions from broad-band seismic signals and its application to the 2004–2005 explosions at Volcán de Colima, Mexico, *Geophys. J. Int.*, 167, 467–478, doi:10.1111/j.1365-246X.2006.03108.x.